PAPER

Exploring the potential of ZnO–Ag@AgBr/SBA-15 Z-scheme heterostructure for efficient wastewater treatment: synthesis, characterization, and real-world applications†

Giang T. T. Pham,[a] Hoa T. Vu,[a] Tham Thi Pham,[a] Nguyen Ngoc Thanh,[a] Van Ngo Thuy,[a] Hung Quang Tran,[b] Huan V. Doan [ID] *[c] and Manh B. Nguyen [ID] *[bd]

This study reports on the synthesis and characterization of ZnO–Ag@AgBr/SBA-15 composites using natural halloysite clay from Yenbai Province, Vietnam, as a silica aluminum source. The synthesized materials demonstrated visible light absorption with a band gap energy range of 2.63–2.98 eV. The dual Z-scheme ZnO–Ag@AgBr/SBA-15 heterojunction exhibited superior catalytic performance compared to ZnO/SBA-15 and Ag@AgBr/SBA-15, owing to its improved electron transfer and reduced electron and hole recombination rate. In particular, the photocatalytic efficiency of ZnO–Ag@AgBr/SBA-15 was evaluated for the removal of harmful phenol red from wastewater under visible light irradiation. The photocatalytic process was optimized by varying the phenol red concentration, pH, and catalyst dosage, and showed that 98.8% of phenol red in 100 mL wastewater (pH = 5.5) can be removed using 40 mg of 20%ZnO–Ag@AgBr/SBA-15 within 120 min. Furthermore, the degradation pathway of phenol red was predicted using liquid chromatographic-mass spectrometry (LC-MS). Finally, the photocatalytic process was successfully tested using water samples collected from the four main domestic waste sources in Hanoi, including the To Lich River, the Hong River, the Hoan Kiem Lake, and the West Lake, demonstrating the high potential of the ZnO–Ag@AgBr/SBA-15 photocatalyst for phenol red degradation in real-world wastewater treatment applications.

1. Introduction

Phenolic compounds find widespread use in various industries, including the production of dyes, pesticides, solvents, explosives, and other industrial precursors.[1–3] However, even in small amounts, these compounds can pose a threat to the environment and human health.[4] To remove such toxic compounds, several techniques like adsorption, catalysis, ozonation, Fenton or photo-Fenton, persulfateoxy oxidation, enhanced oxidation (AOP), and photocatalysis have gained significant research interest.[5–7] Among these methods, photocatalysis has the potential to partially or completely mineralize harmful pollutants like dyes and phenolic compounds into less toxic or benign substances like CO_2 and H_2O.[8,9]

Various semiconductor materials such as ZnO, AgBr, Fe_2O_3, g-C_3N_4, AgBr and TiO_2 have been utilized as photocatalysts.[10,11] Among these, ZnO is a promising candidate due to its superior oxidation resistance, stability, low cost, and non-toxicity, causing no secondary pollution.[12,13] However, the high band gap energy of ZnO (3.3 eV) leads to rapid recombination between holes (h^+) and electrons (e^-) resulting in reduced photocatalytic activity.[14,15] Consequently, researchers have focused on enhancing the efficiency of ZnO by combining it with other semiconductors, using carriers such as graphene, graphene oxide, and carbon nanotubes, doping metals or nonmetals, to reduce band gap energy, and the recombination potential of holes (h^+) and electrons (e^-).[16–18]

One effective approach to improving the photocatalytic performance of ZnO is combining it with AgBr, which enhances the absorption of visible light and reduces electron–hole recombination. For example, Shengnan Liu *et al.*[11] developed a p–n AgBr/ZnO semiconductor that achieved an RhB decomposition efficiency of up to 95.3%, which was nine times higher

[a]Faculty of Chemical Technology, Hanoi University of Industry, 298 Minh Khai, Bac Tu Liem, Ha Noi 10000, Vietnam

[b]Institute of Chemistry, Vietnam Academy of Science and Technology, 18 Hoang Quoc Viet Street, Cau Giay, Ha Noi, Vietnam. E-mail: nguyenbamanh@ich.vast.vn

[c]Department of Mechanical Engineering, University of Bristol, Bristol BS8 1TH, UK. E-mail: huan.doan@bristol.ac.uk

[d]Graduate University of Science and Technology, Vietnam Academy of Science and Technology, 18 Hoang Quoc Viet Street, Cau Giay, Ha Noi, Vietnam

† Electronic supplementary information (ESI) available: FT-IR and EDX spectra of ZnO–Ag@AgBr/SBA-15 samples, Mott–Schottky plot of ZnO/SBA-15 and Ag@AgBr/SBA-15 samples, schematic synthesis of ZnO–Ag@AgBr/SBA-15, UV-vis spectra of phenol red, images of phenol red solution, LC-mass spectra of phenol red, stability of 20%ZnO–Ag@AgBr/SBA-15 sample at different cycles of reaction. See DOI: https://doi.org/10.1039/d3ra01856c

than that of ZnO (10.0%) and AgBr (12.8%) after 120 min of light irradiation. Additionally, Lei Shi *et al.*[19] improved the visible light absorption of ZnO by combining it with AgBr. The RhB removal efficiency reached 35% and 95% after 3 h of reaction with ZnO and AgBr/ZnO photocatalysts, respectively, due to increased light absorption and reduced electron–hole recombination.

Furthermore, incorporating semiconductors with porous materials such as graphene oxide (GO), carbon nanotubes (CNT), metal–organic frameworks (MOFs), and functional silica with high surface area and advanced porosity has been shown to enhance photocatalytic activity by improving the diffusion process and increasing the contact between active sites and reactants.[20,21] Among these materials, Santa Barbara Amorphous-15 (SBA-15) stands out due to its exceptional properties, including high surface area, large pore volume, mechanical and thermal stability. SBA-15 is a mesoporous capillary material with a cubic structure and a pore diameter of 5–10 nm, making it highly valuable for applications in catalysis, adsorption, and environmental treatment.[22] The sol–gel method is typically used to synthesize SBA-15 at highly acidic pH (pH < 1) using silica-containing precursors such as tetraethoxysilane (TEOS), tetramethoxysilane (TMOS), and tetraproxysilane (TPOS).[23] However, these precursors can be costly and harmful, prompting the search for inexpensive and natural sources of silica-containing chemicals. Inspired by previous work, natural halloysite clay from Yenbai Province (Vietnam) was used as a silica aluminum source in the synthesis of ZnO–Ag@AgBr/SBA-15 composites. To optimize the photocatalytic process, the influence of phenol red concentration, catalyst dosage, and pH was studied, along with the phenol red degradation route. Finally, the practical application of the synthesized catalyst was evaluated by testing water samples collected from four major domestic waste sources in Hanoi, including the To Lich River, the Hong River, the Hoan Kiem Lake, and the West Lake.

2. Experimental methods

Chemicals used in this study, including Pluronic P123, cetyltrimethylammonium bromide (CTABr, 98%), sodium hydroxide (NaOH, 98%), hydrochloric acid (HCl, 36%), silver nitrate (AgNO$_3$, 99%), zinc nitrate hexahydrate (Zn(NO$_3$)$_2$·6H$_2$O, 98%) were obtained from Sigma-Aldrich.

2.1 Synthesis of SBA-15

We used halloysite clay minerals from Yenbai Province (Vietnam) to synthesize SBA-15, following a similar method to our previous studies.[23] First, the raw halloysite was calcined at 700 °C for 3 hours and then allowed to cool to ambient temperature. Next, the calcined halloysite was agitated at 80 °C for 24 hours with the addition of 100 mL of 1 M NaOH to obtain a silica precursor for SBA-15 synthesis. The sample was then rinsed with distilled water and dried overnight at 100 °C to remove excess NaOH.

To prepare the SBA-15, a homogeneous solution was created by stirring a mixture of 4 g P123, 30 mL distilled water, and 120 mL 2 M HCl at 40 °C for 3 hours. Next, 4 g of the silica precursor was added and stirred at 600 rpm for 24 hours. The mixture was then gelated at 100 °C for 48 hours, and the resulting white suspension was washed multiple times with H$_2$O to remove P123 and excess HCl. The obtained white solid was crushed and dried at 80 °C for 8 hours, and then calcined at 550 °C for 6 hours to remove the surfactant and obtain the SBA-15.

2.2 Synthesis of ZnO–Ag@AgBr/SBA-15

The sol–gel method was used to synthesize ZnO–Ag@AgBr/SBA-15. Firstly, 0.170 g AgNO$_3$ and 0.364 g CTABr were added to 20 mL H$_2$O and subjected to ultrasonic irradiation for 1 h to obtain solution A. Simultaneously, 0.750 g Zn(NO$_3$)$_2$·6H$_2$O was dissolved in 40 mL of H$_2$O and stirred until a clear solution (solution B) was obtained. Next, 0.7 g SBA-15 was added to 40 mL of C$_2$H$_5$OH and subjected to ultrasonic irradiation for 30 min to create a homogeneous solution (solution C). Subsequently, solutions A and B were slowly dropped into solution C while stirring for 1 h at room temperature and continuing ultrasonic irradiation for 15 min. The mixture was then gel-aged at 80 °C for 24 h and washed multiple times with H$_2$O to eliminate unreacted substances. The material was dried at 80 °C for 8 h and calcined at 500 °C for 5 h to obtain a 20%ZnO–Ag@AgBr/SBA-15 sample. Fig. S1† illustrates the synthesis process of ZnO–Ag@AgBr/SBA-15. Ag@AgBr/SBA-15 and ZnO/SBA-15 samples were synthesized using a similar process as the ZnO–Ag@AgBr/SBA-15 synthesis.

2.3 Characterization

The X-ray diffraction (XRD) patterns were collected using a D8 Advance diffractometer (Germany), with CuKα radiation source ($\lambda = 0.154\ 06$ nm), over the range of 5°–70° 2θ. The morphology of SBA-15 and ZnO–Ag@AgBr/SBA-15 was characterized by scanning electron microscopy (SEM) using JEOL JSM 6500F instrument. Fourier-transform infrared spectroscopy (FTIR) measurements were performed on a Jacos 4700 spectrometer. The surface area of ZnO–Ag@AgBr/SBA-15 photocatalysts was determined by Brunauer–Emmett–Teller (BET) analysis using N$_2$ adsorption on a Tristar-3030 system. The elemental composition of ZnO–Ag@AgBr/SBA-15 and Ag@AgBr/SBA-15 was determined using energy-dispersive X-ray spectroscopy (EDX) on a JEOL JED-2300 spectrometer. Photoluminescence (PL) was measured using a Cary Eclipse fluorescence instrument (Varian), while X-ray photoelectron spectroscopy (XPS) and UV-Vis diffuse reflectance spectroscopy (UV-Vis DRS) were performed using Thermo VG Multilab 2000 and Shimadzu UV2550 spectrophotometers, respectively.

2.4 Photocatalytic testing

The degradation of phenol red using photocatalysts was performed in a 250 mL beaker under the illumination of four 15 W fluorescent lamps. Firstly, 0.4 g L^{-1} of the photocatalysts was added to 100 mL of phenol red solution with a concentration of

10–25 mg L^{-1} and was left to adsorb in the dark for 1 hour to reach adsorption-release equilibrium. The light source power to the surface of the reaction solution was adjusted to 2040 Lux using the four light bulbs (Philips Cleo Compact, 4 lamps, 30 cm, 15 W, Germany), which were placed 15 cm away from the solution and the reaction temperature was maintained at 25 °C by circulating water throughout the reaction. The concentrations of phenol red before and after the reaction were measured using a UV-Vis spectrophotometer (Lambda 35) at an absorption peak of 432 nm.

$$\text{Removal efficiency } (\%) = \frac{C_0 - C_t}{C_0} \times 100 \tag{1}$$

where C_t and C_0 are the concentration at time t and the initial concentration of phenol red, respectively.

Experiments were conducted to investigate other influencing factors, including the concentration of phenol red, pH, catalyst dosage, reactive radicals ($\cdot O_2^-$, h$^+$, $\cdot OH$), and different water sources such as Hoan Kiem Lake, West Lake, Red River, and To Lich River. The experimental procedure was similar to the one described above. To adjust the pH, HCl and NaOH solutions were used for acidic and alkaline conditions, respectively. The wastewater samples were filtered using 2.5 μm filter paper and then mixed with phenol red at a concentration of 20 mg L^{-1}. The degradation products of phenol red were analyzed using mass spectrometry on a Thermo-fisher system (Xevo TQ-XS LC-MS). Chemical oxygen demand and biological oxygen demand were determined using the K$_2$Cr$_2$O$_7$ oxidation method and acid–base titration method, respectively.[24,25]

3. Result and discussion

3.1 Characterization of Ag@AgBr/SBA-15, ZnO/SBA-15 and ZnO–Ag@AgBr/SBA-15 samples

The PXRD patterns of Ag@AgBr/SBA-15, ZnO/SBA-15 and ZnO–Ag@AgBr/SBA-15 composites are presented in Fig. 1.

Fig. 1A indicates that the PXRD of all three samples exhibited peaks at 2θ of 0.85°, 1.6° and 1.84° corresponding to the (100), (110), and (200) reflection planes, respectively.[23,26] The peak intensity at 2θ of 0.85° was high and well-defined, indicating a stable structure and good order of the SBA-15. However, the peak intensity of all samples decreased upon the addition of AgBr and ZnO to SBA-15, suggesting that AgBr and ZnO were dispersed on the capillaries and partially covered the porous structure of the SBA-15 carrier.[23] In Fig. 1B, the large-angle PXRD patterns of the ZnO/SBA-15 sample exhibited peaks at 2θ of 31.355°, 33.8°, 35.76°, 55.8°, 60.8°, 65.5° and 68.15°, which correspond to the (100), (002), (101), (110), (103), (112), and (201) reflection planes and are consistent with the hexagonal wurtzite crystal phase of ZnO (JCPDS Card No. 36-1451).[27] The PXRD pattern of the Ag@AgBr/SBA-15 sample showed peaks at 2θ of 26.7°, 31°, 44.3°, 55°, 64.5°, and 73.4° for the (111), (200), (220), (222), (400), and (420) reflection planes, respectively, which are characteristic of the AgBr phase (JCPDS Card No. 06-0438).[28] The peaks at 2θ of 38.1°, 44.3°, and 64.5° were assigned to the (111), (200), and (220) planes of the Ag metallic phase (JCPDS No. 65-2871). The PXRD diagram of the ZnO–Ag@AgBr/
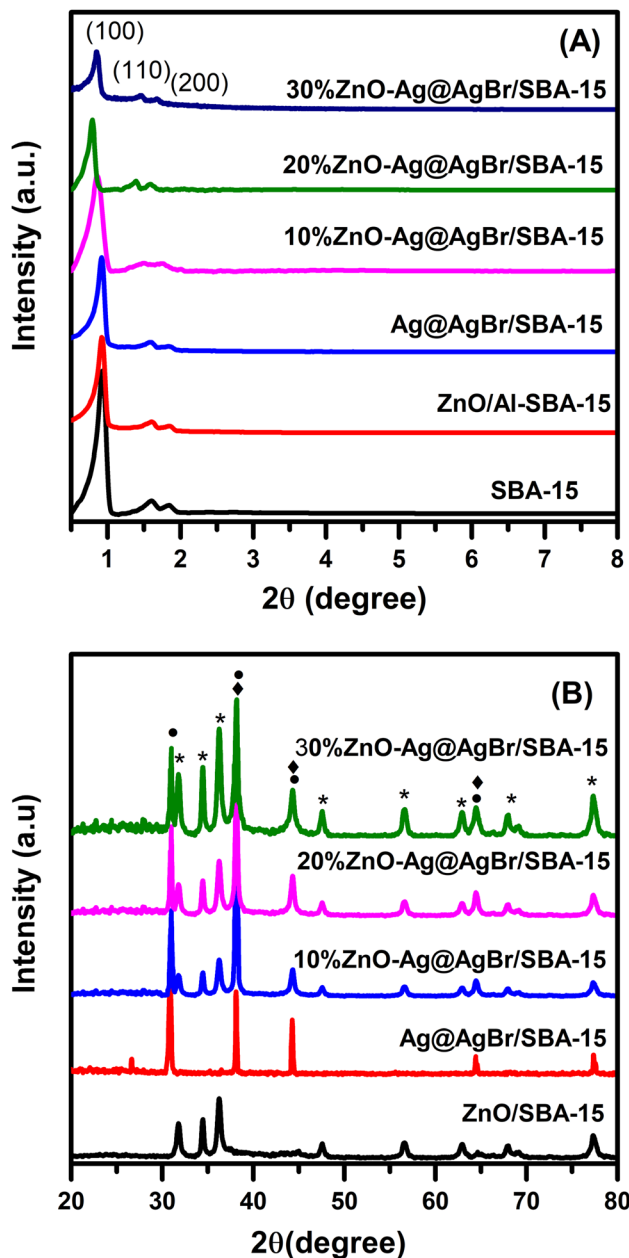

Fig. 1 (A) Small-angle and (B) large-angle XRD patterns of Ag@AgBr/SBA-15, ZnO/SBA-15 and ZnO–Ag@AgBr/SBA-15 samples.

SBA-15 materials showed all the characteristic peaks of the ZnO, Ag, and AgBr phases. The characteristic peak intensity of the ZnO phase in the ZnO–Ag@AgBr/SBA-15 materials increased with increasing ZnO content.

Fig. S2† shows the FTIR spectra of Ag@AgBr/SBA-15, ZnO/SBA-15, and ZnO–Ag@AgBr/SBA-15 composites, where the characteristic peaks at 3433 and 1628 cm^{-1} correspond to the –OH functional groups adsorbed on the materials.[29] The peaks at 1083 and 799 cm^{-1} are characteristic of Si–O–Si bonds, corresponding to symmetry and flexural vibrations, respectively.[30] Additionally, the peaks at 459 and 963 cm^{-1} correspond to prolonged Si–O (tetrahedral) and Si–OH oscillations, respectively.[34] In the ZnO–Ag@AgBr/SBA-15 composite, the peaks at
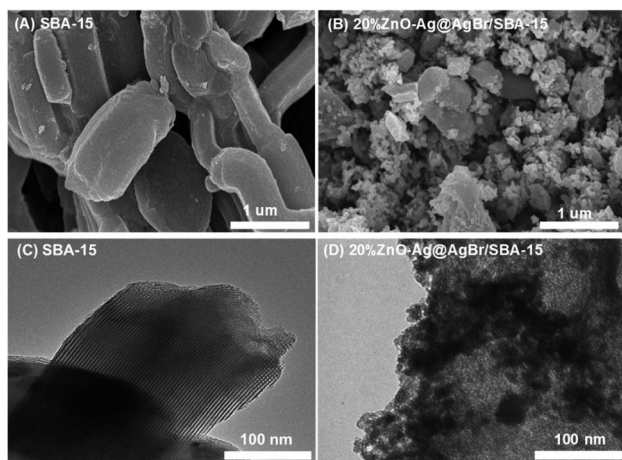
Fig. 2 SEM and TEM images of SBA-15 (A and C) and 20%ZnO–Ag@AgBr/SBA-15 (B and D) samples.

463 and 799 cm^{-1} are broadened due to the superposition of Zn–O stretching vibrations and Si–O–Si peaks. However, the FTIR spectra of Ag@AgBr/SBA-15 and ZnO–Ag@AgBr/SBA-15 composites do not show peaks corresponding to Ag due to the inability of AgNPs to absorb in the infrared region.[31]

The chemical composition of Ag@AgBr/SBA-15 and ZnO–Ag@AgBr/SBA-15 samples was analyzed by EDS, which confirmed the presence of Zn, Ag, O, Si, and C elements without impurities. Table S1† shows that the mass% composition of elements Si, O, Al, Br, and Ag decreases with increased ZnO content on SBA-15. Furthermore, the mass% of ZnO in 10% ZnO–Ag@AgBr/SBA-15, 20%ZnO–Ag@AgBr/SBA-15, and 30% ZnO–Ag@AgBr/SBA-15 composites were 9.1%, 17.5%, and 28.5%, respectively.
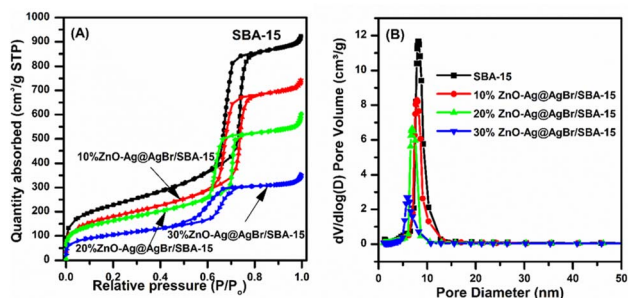

Fig. 3 N$_2$ adsorption–desorption isotherms of ZnO–Ag@AgBr/SBA-15 samples.

Fig. 2 displays SEM and TEM images of the SBA-15 and 20% ZnO–Ag@AgBr/SBA-15 samples. The hexagonal shape of the SBA-15 carrier with an average size of 0.5–1 μm is observed in Fig. 2A. In Fig. 2B, ZnO and AgBr spherical particles with sizes of 20–30 nm are observed on the surface of the SBA-15 carrier. TEM images in Fig. 2C demonstrate the presence of a 2D hexagonal structure with highly ordered parallel arranged capillaries of SBA-15. However, with the loading of AgBr and ZnO in the nanocomposite material, dark regions with a size of 10–30 nm are observed in Fig. 2D, demonstrating that CTABr surfactant was successfully used as a source of bromide to obtain AgBr and ZnO nanoparticles.[19] Additionally, the TEM image (Fig. S3†) of the 30%ZnO–Ag@AgBr/SBA-15 sample demonstrates that ZnO and AgBr particles tend to cluster and agglomerate together into larger size particles (40–100 nm).

N$_2$ adsorption results in Fig. 3 show that all samples possess type IV isotherms according to the IUPAC classification. The hysteresis loop is observed at a relative pressure of 0.5 to 0.7, which is often observed on mesoporous materials.[32] ZnO–Ag@AgBr/SBA-15 samples exhibit a smaller hysteresis loop than that of SBA-15 due to the filling up of ZnO and Ag@AgBr nanoparticles within the SBA-15 capillary, which favors the capillary condensation of N$_2$. Table 1 shows that the SBA-15 carrier sample has the highest surface area (798 m^2 g^{-1}) and pore volume (1.42 cm^3 g^{-1}) and the largest mean diameter (7.14 nm). The increase of ZnO content on the surface of the SBA-15 carrier strongly reduces the surface area, pore volume, and hexagonal pore diameter. Specifically, the surface areas of 10% ZnO–Ag@AgBr/SBA-15, 20%ZnO–Ag@AgBr/SBA-15, and 30% ZnO–Ag@AgBr/SBA-15 composites are 632 m^2 g^{-1}, 568 m^2 g^{-1}, and 368 m^2 g^{-1}, respectively.

Fig. 4A shows the UV-Vis DRS spectrum of the ZnO/SBA-15, Ag@AgBr/SBA-15, and ZnO–Ag@AgBr/SBA-15 composites in the range of 200–780 nm. The ZnO/SBA-15 sample exhibits strong UV absorption with an absorption edge at 400 nm.[33] The Ag@AgBr/SBA-15 sample displays a high absorption region from 200 to 460 nm due to the intrinsic absorption of AgBr, while the visible light absorption region between 600 and 800 nm confirms the presence of Ag nanoparticles, demonstrating the plasmon resonance effect.[34,35] In the ZnO–Ag@AgBr/SBA-15 samples, the light absorption region shifts from the visible light to the UV region with increasing ZnO content.

Tauc plot analysis (Fig. 4B) estimates the band-gap energy of all samples, revealing that the Ag@AgBr/SBA-15 and ZnO/SBA-15 have band-gap energies of about 3.26 and 2.38 eV,

Table 1 Textual characteristics of SBA-15 and ZnO−Ag@AgBr/SBA-15 samples

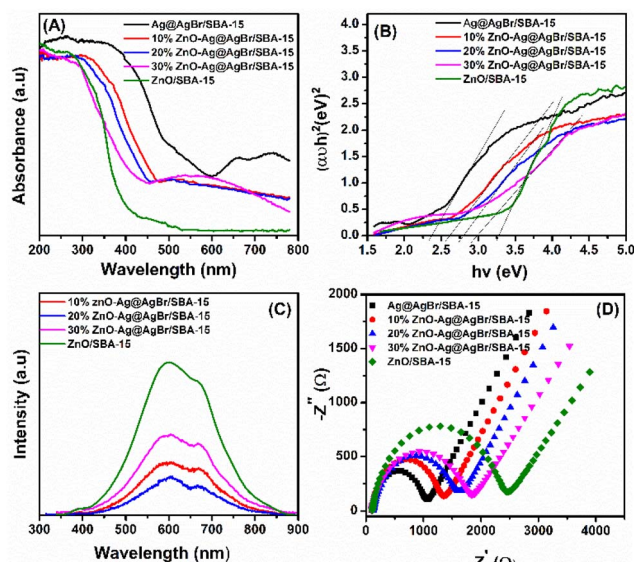| Sample	S_{BET} (m^2 g^{-1})	V_{pore} (cm^3 g^{-1})	D_{BJH} (nm)	E_g (eV)
SBA-15	798	1.42	7.14	—
Ag@AgBr/SBA-15	—	—	—	2.38
10%ZnO−Ag@AgBr/SBA-15	632	1.129	6.99	2.63
20%ZnO−Ag@AgBr/SBA-15	568	0.888	6.32	2.84
30%ZnO−Ag@AgBr/SBA-15	368	0.470	5.56	2.98
ZnO/SBA-15	—	—	—	3.26

Fig. 4 (A) UV-Vis diffuse reflectance spectra; (B) band-gap energies (E_g); photoluminescence spectra (C) and EIS spectra (D) of ZnO–Ag@AgBr/SBA-15 samples.

respectively. The ZnO–Ag@AgBr/SBA-15 sample exhibits a smaller band-gap energy (2.63–2.98 eV) indicating that the formation of heterojunction enhances visible-light absorption. The flat band potential (E_{fb}) was determined by Mott–Schottky (M–S) analysis in 0.1 M Na$_2$SO$_4$ solution (pH 7) in the dark using Ag/AgCl comparison electrodes (Fig. S4†). The E_{fb} values for ZnO/SBA-15 and Ag@AgBr/SBA-15 were found to be −0.87 eV and −0.99 eV (vs. Ag/AgCl at pH 7), respectively. The relationship between the Ag/AgCl electrode and the normal hydrogen electrode (NHE) can be determined using eqn (2).

$$E_{(NHE)} = E_{Ag/AgCl} + 0.059pH + E^{\circ}_{Ag/AgCl} \qquad (2)$$

where $E^{\circ}_{Ag/AgCl} = 0.1976$ V at 25 °C and $E_{Ag/AgCl}$ is the working potential.

The flat band potentials (E_{fb}) for Ag@AgBr/SBA-15 and ZnO/SBA-15 were determined to be −0.26 eV and −0.38 eV vs. NHE, respectively. For n-type semiconductors, the conduction band (CB) edge is set at 0.2 eV above the flat band (E_{fb}),[36] resulting in CB values of −0.58 eV and −0.46 eV for the Ag@AgBr/SBA-15 and ZnO/SBA-15 samples, respectively. The valence band positions can be estimated based on the relation between the conduction band (E_{CB}) and band gap energy (E_g):

$$E_{VB} = E_g + E_{CB} \qquad (3)$$

The VB potentials of ZnO/SBA-15 and Ag@AgBr/SBA-15 samples were identified to be 2.8 eV and 1.78 eV, respectively.

The PL technique was used to investigate the cleavage and recombination of photonic excitons in the ZnO/SBA-15, Ag@AgBr/SBA-15, and ZnO–Ag@AgBr/SBA-15 composites. The luminescence spectra of these materials were recorded in the range of 350–900 nm and are presented in Fig. 4C. The ZnO/SBA-15 sample exhibited two main luminescence peaks at

600 nm and 680 nm.[37] The broad luminescence peak at 600 nm indicates the recombination of conduction band electrons with double ionized oxygen vacancies located below the CB edge. The high emission intensity of ZnO/SBA-15 indicates rapid recombination of e$^-$/h$^+$ pairs in this sample.[38] However, when ZnO was combined with AgBr, the intensity of the PL spectrum decreased significantly, indicating a reduction in electron–hole recombination in the composite material. The hybridization of ZnO nanostructures with AgBr can trap electrons, leading to lower electron–hole recombination and improved optical properties of the material.[37]

The EIS method was used to determine the charge transfer rates of the ZnO/SBA-15, Ag@AgBr/SBA-15, and ZnO–Ag@AgBr/SBA-15 samples. Fig. 4D shows that the smallest Ag@AgBr/SBA-15 semicircle indicates the fastest charge transfer rate, while the largest semicircle for the ZnO/SBA-15 sample indicates the lowest charge transfer rate. Loading Ag@gBr nanoparticles onto the ZnO surface improved the charge transfer rate of the ZnO–Ag@AgBr/SBA-15 samples.[34] UV-Vis DRS, EIS, and PL measurements showed that the ZnO–Ag@AgBr/SBA-15 sample had (i) a shifted light absorption region and increased visible light absorption enhancement, (ii) reduced recombination between the hole and the electric charge, and (iii) faster charge transfer.

The surface composition and chemical state of Ag@AgBr/SBA-15, ZnO/SBA-15, and 20%ZnO–Ag@AgBr/SBA-15 samples were investigated using the XPS method (Fig. 5 and S5†). The full-scan XPS spectra in Fig. S4† (20%ZnO–Ag@AgBr/SBA-15) show the presence of Si, C, O, Br, Ag, and Zn elements with binding energies of 103, 285, 533, 68, 368, and 1022 eV, respectively.[39] Similarly, the full-scan XPS spectra of the Ag@AgBr/SBA-15 sample (Fig. S4A†) show the existence of elements Si, C, O, Al, Br, and Ag. In Fig. 5A–C, the high-resolution XPS spectra O 1s of Ag@AgBr/SBA-15, ZnO/SBA-15, and ZnO–Ag@AgBr/SBA-15 samples fluctuate at energies 532.96 eV assigned to M–O (M = Si, Zn). The Ag@AgBr/SBA-15 and ZnO–Ag@AgBr/SBA-15 samples have binding energies of 373.8 eV and 367.8 eV for Ag 3d$_{3/2}$ and Ag 3d$_{5/2}$, respectively (Fig. 5D and E).[23] The high-resolution XPS spectra of Zn 2p show two energy peaks at 1044.2 eV and 1020.9 eV which are assigned
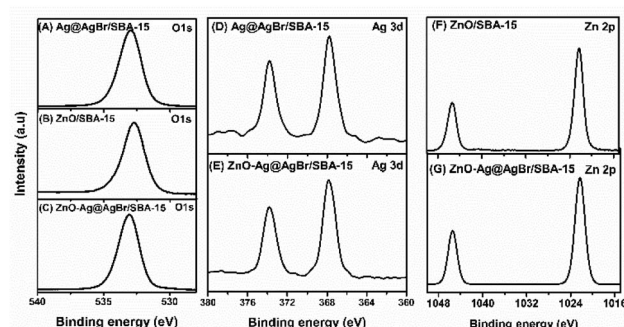

Fig. 5 High-resolution O 1s XPS spectra of Ag@AgBr/SBA-15 (A), ZnO/SBA-15 (B) and 20%ZnO–Ag@AgBr/SBA-15 (C), high-resolution Ag 3d XPS spectra of Ag@AgBr/SBA-15 (D) and 20%ZnO–Ag@AgBr/SBA-15 (E) high-resolution Zn 2p XPS spectra of ZnO/SBA-15 (F) and 20% ZnO–Ag@AgBr/SBA-15 (G).

to Zn $2p_{1/2}$ and Zn $2p_{3/2}$ in the ZnO/SBA-15 and ZnO–Ag@AgBr/SBA-15 samples, respectively.[40] The binding energy of Ag 3d in the ZnO–Ag@AgBr/SBA-15 sample decreased compared with that of Ag@AgBr/SBA-15, while the binding energy of O 1s and Zn 2p in the ZnO/SBA-15 sample increased. These results indicate that Ag metal facilitates efficient electron transport between AgBr and ZnO.[35]

3.2 Photocatalytic activity of Ag@AgBr/SBA-15, ZnO/SBA-15 and 20%ZnO–Ag@AgBr/SBA-15 samples

Fig. 6 presents the photocatalytic activities of Ag@AgBr/SBA-15, ZnO/SBA-15, and ZnO–Ag@AgBr/SBA-15 samples. It is observed that there is little or no reactivity in the presence of visible light without photocatalyst, with only 1–2% of phenol red degraded within 120 minutes. In contrast, approximately 2–4% of phenol red is removed in the dark for 60 minutes, suggesting negligible adsorption. These findings are consistent with those reported by Wong *et al.*[41] After irradiation for 120 minutes, the decomposition efficiencies are 52.8%, 63.2%, 90.3%, 98.8%, and 95.8% for ZnO/SBA-15, Ag@AgBr/SBA-15, 10%ZnO–Ag@AgBr/SBA-15, 20%ZnO–Ag@AgBr/SBA-15, and 30%ZnO–Ag@AgBr/SBA-15, respectively. Notably, the removal efficiency of ZnO–

Ag@AgBr/SBA-15 photocatalysts is significantly higher than that of Ag@AgBr/SBA-15 and ZnO/SBA-15, owing to the enhanced visible light absorption, reduced electron–hole recombination, and increased charge transfer rate, as demonstrated in the previous Fig. 4 results. The photocatalyst with 20% ZnO loading in ZnO–Ag@AgBr/SBA-15 has the highest removal efficiency of phenol red (98.8%). However, the 30% ZnO–Ag@AgBr/SBA-15 sample, with a larger crystalline size of particle sizes ranging from 40–100 nm, tended to agglomerate into larger sized particles due to an excess of ZnO. This resulted in a reduced surface area and separation efficiency of the charge carriers, leading to a decreased phenol red removal efficiency (95.8%). Therefore, the crystalline size of the material significantly influences the photocatalytic properties of the ZnO–Ag@AgBr/SBA-15 sample, where a smaller crystalline size with uniform distribution of ZnO and AgBr nanoparticles enhances the catalytic activity for phenol degradation.[11] The performance of 20%ZnO–Ag@AgBr/SBA-15 in removing phenol red can be influenced by contamination concentration, catalyst dosage, and pH, as shown in Fig. 6B–D. The removal rate gradually decreased from 99.4% to 91.5% when the initial phenol red concentration increased from 10 to 25 mg L^{-1} (Fig. 6B and Table S2†).

We chose a concentration of 20 mg L^{-1} for further investigation. The surface area of the 20%ZnO–Ag@AgBr/SBA-15 material is influenced by pH values (Fig. S6†), and the material isoelectric point (IEP) is 7.4. When the pH value decreased from 9 to 3 (Fig. 6C and Table S2†), the decomposition rate of phenol red after 120 min of visible light irradiation increased from 72.4% to 99.2%. The phenol red removal rate increases at pH < 7.4 but reduces at pH > 7.4 due to the difficulty of sulfonic and phenol anions in accessing the negatively charged 20% ZnO–Ag@AgBr/SBA-15 surface. In Fig. 6D, the dose of photocatalyst 20%ZnO–Ag@AgBr/SBA-15 affects the efficiency of phenol red degradation. Specifically, when reducing the initial concentration of the catalyst from 0.5 to 0.2 g L^{-1}, the phenol red removal efficiency decreases from 99.4% to 87.6% after 120 minutes of light irradiation. This decrease occurs due to a reduction in the catalyst mass and a decrease in the ratio of active sites, resulting in a reduction in catalytic activity. The optimal conditions were found to be 20 mg L^{-1} phenol red, 0.4 g L^{-1} 20%ZnO–Ag@AgBr/SBA-15, and pH 5. The UV-Vis spectrum in Fig. S7† showed a decrease in intensity at 290 and 432 nm wavelengths of phenol red in water, indicating the decomposition of phenol red into other intermediate compounds (Table S3†). The color of the phenol red solution gradually changed to a transparent color with increased light irradiation time (Fig. S8†). The TOC, BOD5, and COD of the photocatalytic degradation of phenol red on the 20%ZnO–Ag@AgBr/SBA-15 photocatalyst were 69.86%, 73.38%, and 43.32%, respectively, after 120 minutes of irradiation. The 20%ZnO–Ag@AgBr/SBA-15 composite exhibited superior phenol red treatment efficiency compared to other catalyst materials, such as TiO_2, ZnO, goethite (α-FeOOH), Nb(2.0)/TiO_2, and CuO/ZnO/TiO_2 (Table S3†). The stability of 20%ZnO–Ag@AgBr/SBA-15 was presented in Fig. S9,† showing that phenol red removal efficiency remained high after 5 cycles of reaction. The morphological
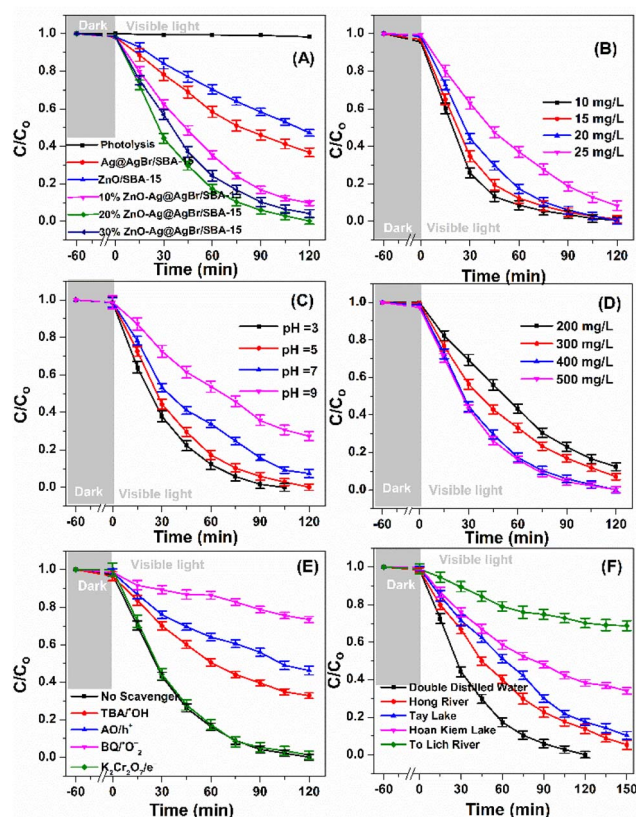

Fig. 6 C/C_0 as a function of reaction time over Ag@AgBr/SBA-15, ZnO/SBA-15 and ZnO–Ag@AgBr/SBA-15 samples (A), C/C_0 as a function of reaction time over 20%ZnO–Ag@AgBr/SBA-15 at different phenol red concentrations (B), pH value (C), amount of photocatalysts (D), reaction radical trap experiments (E) and phenol red in different types of natural surface water (F). Phenol red concentration of 20 mg L^{-1}, catalyst dosage 0.4 g L^{-1}, pH = 5.

stability and phase state of the 20%ZnO–Ag@AgBr/SBA-15 sample after five reaction cycles were evaluated using XRD and SEM-TEM methods. The TEM, SEM images, and XRD patterns (Fig. S10 and S11†) showed no significant change in the phase structure and morphology of the 20%ZnO–Ag@AgBr/SBA-15 sample after five reaction cycles. These results demonstrate the stability and reusability of this sample after five cycles of phenol red photodegradation.
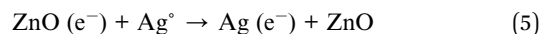
3.3 Mechanism

Based on the optimal conditions for the photocatalyst 20%ZnO–Ag@AgBr/SBA-15, we investigated the effects of reactive radicals ($^{\cdot}OH$, $^{\cdot}O_2^-$), holes (h^+), and electrons (e^-) in the degradation of phenol red. To capture the reactive radicals, we used radical scavengers including potassium dichromate ($K_2Cr_2O_7$), *tert*-butanol (TBA), ammonium oxalate monohydrate (AO), and 1,4-benzoquinone (BQ). As shown in Fig. 6E and Table S2,† the removal efficiency of phenol red reached 98.8% when no reactive radical scavengers were used. However, when TBA, AO, and BQ were added, the removal efficiency of phenol red decreased to 65.16%, 51.05%, and 24.35%, respectively, after 120 minutes of light irradiation. On the other hand, when $K_2Cr_2O_7$ was added, the removal efficiency of phenol red reached 96.38%. These results indicate that $^{\cdot}OH$, $^{\cdot}O_2^-$, and h^+ were the dominant reactive species, and $^{\cdot}O_2^-$ played the most crucial role in the photodegradation of phenol red on the ZnO–Ag@AgBr/SBA-15 catalyst.

Based on our electrochemical measurements and the role of radicals in phenol red removal, we propose a photocatalytic mechanism for the ZnO–Ag@AgBr/SBA-15 photocatalyst. We hypothesize a Z-scheme mechanism to describe the separation processes of electron–hole pairs based on the VB and CB structures of the Ag@AgBr/SBA-15 and ZnO/SBA-15 samples (Fig. 7). When exposed to light energy greater than the band gap energy of the material, holes and electrons are generated as described in eqn (4).

$$ZnO–Ag@AgBr/SBA\text{-}15 + h\nu \rightarrow$$
$$ZnO–Ag@AgBr/SBA\text{-}15 \ (h^+ + e^-) \quad (4)$$
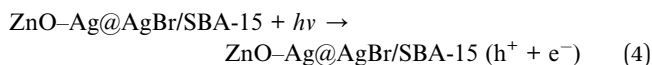
Next, the electrons on the CB of ZnO transfer to Ag, and further migrate to the VB of AgBr to recombine with the h^+ of AgBr (eqn (5) and (6)).[34]

Fig. 7 (A) Schematic of the separation transfer before contact, and (B) possible Z-scheme transfer in the 20%ZnO–Ag@AgBr/SBA-15 photocatalyst.

$$ZnO \ (e^-) + Ag^\circ \rightarrow Ag \ (e^-) + ZnO \quad (5)$$

$$Ag^\circ \ (e^-) + AgBr \ (h^+) \rightarrow \text{photons and/or heart} \quad (6)$$

At the same time, the holes that remain in the VB of ZnO can directly oxidize pollutants or react with H_2O to produce $^{\cdot}OH$. This is because the VB of ZnO (2.8 eV) is more positive than the standard potential of $^{\cdot}OH/H_2O$ (2.40 eV) (as shown in eqn (7)).

$$ZnO \ (h^+) + H_2O \rightarrow {^{\cdot}OH} + H^+ \quad (7)$$

At the CB of AgBr, electrons can reduce O_2 to $^{\cdot}O_2^-$ because the CB of AgBr (−0.58 eV) is more negative than the standard potential of $O_2/^{\cdot}O_2^-$ (−0.33 eV). The resulting $^{\cdot}O_2^-$ can continue to perform the decomposition reaction of phenol red into less toxic products (eqn (8)).

$$O_2 + AgBr \ (e^-) \rightarrow {^{\cdot}O_2^-} \quad (8)$$
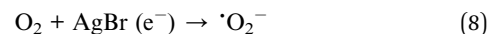
Finally, radicals such as $^{\cdot}O_2^-$, h^+ and $^{\cdot}OH$ can oxidize phenol red to less toxic products (eqn (9)).

$${^{\cdot}O_2^-}, h^+ \text{ and } {^{\cdot}OH} + \text{phenol red} \rightarrow \text{degraded products} \quad (9)$$

Furthermore, the SBA-15 support with its large surface area and wide capillary diameter can act as an electron trap during the photocatalytic decomposition on ZnO–Ag@AgBr/SBA-15. The electrons generated in AgBr and ZnO can diffuse and migrate to the SBA-15 support and react with O_2 on the surface of ZnO–Ag@AgBr/SBA-15, producing $^{\cdot}O_2^-$ radicals.[32]

3.4 Treatment of phenol red in different water environments

The photocatalyst 20%ZnO–AgBr/SBA-15 was tested for its ability to remove phenol red from various domestic wastewater sources in Hanoi (Vietnam), including the Hoan Kiem Lake, the West Lake, the Red River, and the To Lich River. Fig. 6F shows that the 20%ZnO–AgBr/SBA-15 sample was able to remove phenol red from water samples collected from the Hong River, the To Lich River, the Hoan Kiem Lake, and the West Lake, with removal efficiencies of 94.7%, 31.1%, 69.6%, and 89.8%, respectively, after 150 minutes of reaction.[42] However, the treatment efficiency of the To Lich River was only 31.1%, which may be attributed to the presence of multiple organic and inorganic substances in the water source that hindered the decomposition of phenol red. Additionally, natural colloidal particles with sizes ranging from 1 nm to 1 μm were found in this water sample and could adsorb on the surface of the catalyst, hindering the contact between phenol red and the ZnO–AgBr sites in the catalyst.

3.5 Decomposition pathway of phenol red using the 20% ZnO–Ag@AgBr/SBA-15 composite

This study employed LC-MS to determine the intermediate products (Fig. S12 and Table S4†) and propose a mechanism for the degradation reaction of phenol red (Fig. 8). The ionic signal at *m/z* 355.03 in Fig. S8† corresponds to phenol red. As the irradiation time increases, the intensity of this signal decreases,
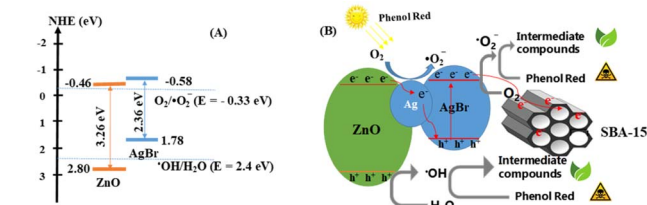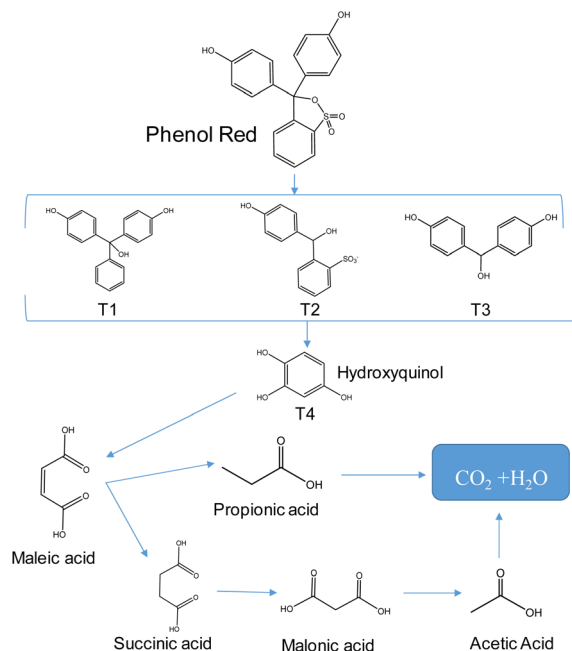
Fig. 8 The possible decomposition pathway of phenol red in the 20% ZnO–Ag@AgBr/SBA-15 system.

indicating the decomposition of phenol red and the introduction of radicals such as $\cdot O_2^-$, $\cdot OH$, and holes (h^+) in divinyl sulfate cleavage and fragment cleavage. This process produces various intermediate products, including T1 (m/z 290.24), T2 (m/z 279.03), T3 (m/z 216.35), and T4 (m/z 126.81). These intermediate compounds then participate in ring-opening reactions to form maleic acid (m/z 116.16) intermediates,[43,44] which are subsequently oxidized to smaller molecules like malonic acid (104.05), propionic acid (m/z 74.04), and acetic acid (m/z 60.04) before finally being mineralized to H_2O and CO_2.[45]

4. Conclusions

In this study, we produced ZnO–Ag@AgBr/SBA-15 composites using halloysite clay as a silica aluminum source and the sol–gel method. These composites exhibited excellent photocatalytic activity, with a band gap energy of 2.63–2.98 eV, reduced electron and hole recombination rate, and increased electron transmission and separation rate. Under visible light irradiation, the 20%ZnO–Ag@AgBr/SBA-15 composite showed remarkable phenol red removal efficiency (98.8%) compared to ZnO/SBA-15 (52.8%) and Ag@AgBr/SBA-15 (63.2%) materials. After 120 min of irradiation, the values of TOC, BOD5, and COD of the photocatalytic degradation of phenol red on the 20% ZnO–Ag@AgBr/SBA-15 photocatalyst were 69.86%, 73.38%, and 43.32%, respectively.

We examined the phenol red concentration, pH, and catalyst dosage as parameters impacting the photocatalytic process. Additionally, we used different wastewater sources (To Lich River, Hong River, Hoan Kiem Lake, and West Lake) to evaluate the performance of the 20%ZnO–Ag@AgBr/SBA-15 composite. The results showed that this catalyst was highly effective in

removing phenol red from the Hong River (94.7%), Hoan Kiem Lake (69.6%), and West Lake (89.8%). Moreover, we predicted the degradation pathway of phenol red using liquid chromatographic-mass spectrometry (LC-MS), which can promote future studies.

Author contributions

Giang T. T. Pham: investigation, formal analysis, data curation, writing – original draft. Hoa T. Vu: conceptualization, investigation, formal analysis, data curation. Tham Thi Pham: conceptualization, investigation, formal analysis, data curation. Nguyen Ngoc Thanh: conceptualization, investigation. Van Ngo Thuy: investigation, formal analysis, data curation. Tran Quang Hung: conceptualization, investigation, formal analysis, data curation. Huan V. Doan: conceptualization, investigation, data curation, writing – reviewing and editing, Manh B. Nguyen: investigation, formal analysis, data curation, writing – original draft and reviewing and editing.

Conflicts of interest

There are no conflicts to declare.

Acknowledgements

References

1 H. S. Wahab and A. A. Hussain, *J. Nanostruct. Chem.*, 2016, **6**, 261–274.
2 V. T. T. Ha, M. B. Nguyen, T. N. Tam, V. T. Thu, P. T. H. Yen, P. H. Phong, D. N. Nhiem, L. Q. Hung and T. Q. Hai, *J. Appl. Electrochem.*, 2022, **52**, 607–616.
3 M. B. Nguyen, N. H. Anh, V. T. Thu, P. Thi, H. Yen, P. H. Phong, L. Q. Hung, N. Thi, T. Ngan, T. Q. Hai, V. Thi and T. Ha, *RSC Adv.*, 2022, 33825–33834.
4 M. B. Nguyen, V. T. Hong Nhung, V. T. Thu, D. T. Ngoc Nga, T. N. Pham Truong, H. T. Giang, P. T. Hai Yen, P. H. Phong, T. A. Vu and V. T. Thu Ha, *RSC Adv.*, 2020, **10**, 42212–42220.
5 M. Norouzi, A. Fazeli and O. Tavakoli, *J. Water Process. Eng.*, 2020, **37**, 101489.
6 N. Mojoudi, N. Mirghaffari, M. Soleimani, H. Shariatmadari, C. Belver and J. Bedia, *Sci. Rep.*, 2019, **9**, 1–12.
7 K. Miserli, D. Kogola, I. Paraschoudi and I. Konstantinou, *Chem. Eng. J. Adv.*, 2022, **9**, 100201.
8 M. B. Nguyen, D. T. Sy, V. T. K. Thoa, N. T. Hong and H. V. Doan, *J. Taiwan Inst. Chem. Eng.*, 2022, **140**, 104543.
9 X. Sun, C. Wang, D. Su, G. Wang and Y. Zhong, *Adv. Mater. Technol.*, 2020, **5**, 1–15.
10 D. Van Le, M. B. Nguyen, P. T. Dang, T. Lee and T. D. Nguyen, *RSC Adv.*, 2022, **12**, 22367–22376.
11 S. Liu, M. Zheng, R. Chen and Z. Wang, *RSC Adv.*, 2017, 7, 31230–31238.

12 C. Bogatu, M. Covei, I. Polo-Lopez, A. Duta and S. Malato, *Catal. Today*, 2023, **413–415**, 113947.

13 S. B. Shinde, S. D. Dhengale, O. S. Nille, S. S. Jadhav, A. H. Gore, T. R. Bhosale, N. B. Birajdar, S. S. Kolekar, G. B. Kolekar and P. V. Anbhule, *Inorg. Chem. Commun.*, 2023, **147**, 110242.

14 H. Ghannam, J. P. B. Silva and A. Chahboun, *RSC Adv.*, 2021, **11**, 23346–23354.

15 M. R. Alenezi, A. M. Almeshal and A. N. Alkhaledi, *Mater. Adv.*, 2022, 6577–6583.

16 K. Flores, C. Valdes, D. Ramirez, T. M. Eubanks, J. Lopez, C. Hernandez, M. Alcoutlabi and J. G. Parsons, *Chemosphere*, 2020, **259**, 127414.

17 N. Arsalani, S. Bazazi, M. Abuali and S. Jodeyri, *J. Photochem. Photobiol., A*, 2020, **389**, 112207.

18 L. A. Calzada, R. Castellanos, L. A. García and T. E. Klimova, *Microporous Mesoporous Mater.*, 2019, **285**, 247–258.

19 L. Shi, L. Liang, J. Ma and J. Sun, *Superlattices Microstruct.*, 2013, **62**, 128–139.

20 G. D. Mihai, V. Meynen, M. Mertens, N. Bilba, P. Cool and E. F. Vansant, *J. Mater. Sci.*, 2010, **45**, 5786–5794.

21 A. Ehsani, M. Bigdeloo, H. Alamgholiloo, E. Asgari, A. Sheikhmohammadi, S. Nazari, B. Hashemzadeh and N. Ghasemian, *J. Energy Storage*, 2022, **50**, 104633.

22 M. Kruk, M. Jaroniec, C. H. Ko and R. Ryoo, *Chem. Mater.*, 2000, **12**, 1961–1968.

23 X. N. Pham, M. B. Nguyen, H. S. Ngo and H. V. Doan, *J. Ind. Eng. Chem.*, 2020, **90**, 358–370.

24 K. Byrappa, A. K. Subramani, S. Ananda, K. M. Lokanatha Rai, R. Dinesh and M. Yoshimura, *Bull. Mater. Sci.*, 2006, **29**, 433–438.

25 U. Younas, S. Iqbal, A. Saleem, M. Iqbal, A. Nazir, S. Noureen, K. Mehmood and N. Nisar, *Acta Ecol. Sin.*, 2017, **37**, 236–239.

26 X. N. Pham, M. B. Nguyen and H. V. Doan, *Adv. Powder Technol.*, 2020, **31**, 3351–3360.

27 V. P. Dinesh, P. Biji, A. Ashok, S. K. Dhara, M. Kamruddin, A. K. Tyagi and B. Raj, *RSC Adv.*, 2014, **4**, 58930–58940.

28 J. He, D. W. Shao, L. C. Zheng, L. J. Zheng, D. Q. Feng, J. P. Xu, X. H. Zhang, W. C. Wang, W. H. Wang, F. Lu, H. Dong, Y. H. Cheng, H. Liu and R. K. Zheng, *Appl. Catal., B*, 2017, **203**, 917–926.

29 C. Thunyaratchatanon, W. Sinsakullert, A. Luengnaruemitchai and K. Faungnawakij, *Biomass Convers. Biorefin.*, 2021, **11**, 1733–1747.

30 S. T. Pham, M. B. Nguyen, G. H. Le, T. D. Nguyen, C. D. Pham, T. S. Le and T. A. Vu, *Chemosphere*, 2021, **265**, 129062.

31 Y. Chi, Q. Yuan, Y. Li, J. Tu, L. Zhao, N. Li and X. Li, *J. Colloid Interface Sci.*, 2012, **383**, 96–102.

32 M. B. Nguyen, X. N. Pham and H. V. Doan, *RSC Adv.*, 2021, **11**, 31738–31745.

33 N. Zhang, S. Xie, B. Weng and Y. J. Xu, *J. Mater. Chem. A*, 2016, **4**, 18804–18814.

34 S. Huang, Y. Xu, M. Xie, Q. Liu, H. Xu, Y. Zhao, M. He and H. Li, *RSC Adv.*, 2017, **7**, 30845–30854.

35 Y. Yue, K. Hou, J. Chen, W. Cheng, Q. Wu, J. Han and J. Jiang, *ACS Appl. Mater. Interfaces*, 2022, **14**, 24708–24719.

36 A. Kumar, S. K. Sharma, G. Sharma, C. Guo, D. V. N. Vo, J. Iqbal, M. Naushad and F. J. Stadler, *J. Hazard. Mater.*, 2021, **402**, 123790.

37 G. Jayalakshmi, K. Saravanan, J. Pradhan, P. Magudapathy and B. K. Panigrahi, *J. Lumin.*, 2018, **203**, 1–6.

38 A. B. Lavand and Y. S. Malghe, *J. Saudi Chem. Soc.*, 2015, **19**, 471–478.

39 T. S. Miller, A. B. Jorge, T. M. Suter, A. Sella, F. Corà and P. F. McMillan, *Phys. Chem. Chem. Phys.*, 2017, **19**, 15613–15638.

40 P. Dai, T. Tao Yan, X. xin Yu, Z. man Bai and M. Zai Wu, *Nanoscale Res. Lett.*, 2016, **11**, 226.

41 A. R. Mohamed, C. L. Wong and Y. N. Tan, *J. Nanotechnol.*, 2011, 904629.

42 N. Trung Dung, N. Hoang Duc, V. Thai Binh, V. Dinh Thao, M. B. Nguyen, L. Viet Ngan and N. Nhat Huy, *Sep. Purif. Technol.*, 2021, **285**, 120358.

43 Y. Liu, Y. Zhu, J. Xu, X. Bai, R. Zong and Y. Zhu, *Appl. Catal., B*, 2013, **142–143**, 561–567.

44 L. Baia, A. Vulpoi, T. Radu, É. Karácsonyi, A. Dombi, K. Hernádi, V. Danciu, S. Simon, K. Norén, S. E. Canton, G. Kovács and Z. Pap, *Appl. Catal., B*, 2014, **148–149**, 589–600.

45 M. M. M'Arimi, C. A. Mecha, A. K. Kiprop and R. Ramkat, *Renewable Sustainable Energy Rev.*, 2020, **121**, 109669.